

Synergistic Effects of Advanced MoSe₂/MnO₂ Nanocomposite for Direct yellow dye degradation for Enhanced photocatalytic Applications

Gokulnath Dhanasekaran ^a, Nisha Parthiban ^a, Nithya. N ^b, D. Karthigaimuthu ^a,
G. Vijayakumar ^b, Sambasivam Sangaraju ^c, Elangovan Tangavel ^{a *}

^a Smart Energy Materials Research Laboratory (SEMRL), Department of Energy Science and Technology, Periyar University, Salem, India-636011

^b Department of Physics, PSG College of arts and Science, Coimbatore, India

^c National Water and Energy Center, United Arab Emirates University, Al Ain, 15551, UAE

Abstract

MoSe₂, a significant component within the class of two-dimensional transition metal dichalcogenides (TMDCs), boasts a diverse set of photocatalysis characteristics. Herein, we report a simple hydrothermal technique to synthesis MoSe₂/MnO₂ nanocomposites with controllable morphologies size with enhanced photocatalytic activity. The obtained nanocomposite was confirmed by the analysed peaks of MoSe₂/MnO₂ observed in Powder X-ray diffraction (13.6°, 18.1°, 37.5°), infrared spectra (495 cm⁻¹, 645 cm⁻¹, 1410 cm⁻¹), UV-Vis spectra (506 nm, 640 nm, 748 nm) and the narrowing band gap 1.96 eV, 2.52 eV and 2.73 eV. Due to the efficient separation of photogenerated electron-hole pairs facilitated by the rapid transfer of photogenerated electrons by the addition of MnO₂, the MoSe₂/MnO₂ composite demonstrates significantly enhanced solar-driven photocatalytic performance and excellent stability in degrading Direct Yellow (DY), a common pollutant found in industrial effluents. The MoSe₂/MnO₂ nanocomposite photocatalytic activity was found to be 1.2 to 1.6 times higher than that of its individual components of MoSe₂ and MnO₂, indicating synergistic effects leading to enhanced performance. This underscores its considerable potential for environmental remediation, offering a promising approach for the degradation of harmful industrial chemicals present in wastewater using sunlight.

Keywords Molybdenum diselenide; Manganese dioxide; Nanocomposite; Photocatalysis; UV-Vis light

1. Introduction

Energy exhaustion and environmental pollution are two major issues hindering the sustainable and healthy development of human civilisation in the 21st century, passing a threat to human life due to the rapid economic expansion [1–5]. When the toxic substances produced by industries and human activities mixed with the ground and water which leads to pollute vegetation, and food web. It can have a devastating effect on human and environmental health. Luckily, photocatalytic technology can harness limitless solar energy for clean, renewable power, which may help mitigate the greenhouse impact while simultaneously addressing and reducing fossil fuel depletion [6–9]. Among the many approaches for cleaning up polluted environment, photocatalytic technology is gaining more importance. [10–13]. Due to its enormous potential for purifying both air and water. Photocatalytic materials need inherent optical and electrical characteristics to determine their photocatalytic capabilities, which are critical in photocatalytic processes [14–16].

A wide variety of uses have been considered for MoSe₂ because of its outstanding chemical stability, large surface area, and narrow band gap, they have used as lubricants, photovoltaics, catalysis, and electrodes in high energy density batteries & supercapacitors [17]. mechanical, chemical, and physical methods such as, chemical vapour deposition, mechanical exfoliation, hydrothermal, solvothermal, and the colloidal approaches were widely used to prepare MoSe₂ [17–19]. A typical 2D lamellar crystal of MoSe₂ that allows valance band electrons excited to conduction band easily using the visible region of light. In this investigation we have carried out simple hydrothermal technique to prepare MoSe₂ nanoparticles. Since this process does not require catalyst, seed, or harmful surfactants, it is simpler, cheaper, and allows for more control over growth of nanostructure compared to other traditional approaches [20–22]. Hydrothermal processing technique improves nanoparticle size and nucleation homogeneity, enabling direct sample extraction from the solution. the limited photocatalytic efficiency of MoSe₂ is due to poor conductivity, slow charge transfer process, non-porous nature and the photogenerated electron-hole pairs are likely to recombinate, which restricts the efficiency of the material [23]. Conductive materials, such as metal oxides, carbon nanotubes, or conducting polymers, may interact with MoSe₂ to lower their resistance [23,24].

Among the various types of oxide phases, like manganese dioxide (MnO₂) is one type of transition metal oxide that stands out as an n-type semiconductor with a unique two-

dimensional layered structure. Manganese dioxide (MnO_2) nanostructures, which also a visible light acceptor. Weak Van der Waals interactions link layers of manganese (Mn) and oxygen (O) atoms through covalent bonds in the structure. The multi-layered structure of MnO_2 gives it useful properties in many contexts of photocatalysis. Especially its band gap in the visible range, and unique layered structure enables strong photo absorption by means of multireflection of incident light on the surface. It also enables efficient layer-by-layer transport of reactants, intermediates, and products. Given its appropriate band gap energy within the visible light range, and its structural advantages presents MnO_2 as a promising option for catalyst applications. It is possible to increase the overall efficiency of photocatalysis by combining MnO_2 with Transition metal dichalcogenides (TMDCs) photocatalysts. Researchers like V.K. Parida, et al and his coworkers [25,26] have successfully composited Bi_2O_3 with zinc oxide MnO_2 photocatalysts to achieve improved photocatalytic activity. Due to better charge transfer process between heterojunctions between two semiconducting materials which leads to improving overall performance, since MnO_2 is an excellent oxide semiconductor for photocatalysis and other application in catalysis, we have chosen it for heterojunction with MoSe_2 .

The present study has demonstrated a novel category of photocatalytic materials based on nanocomposites, specifically the $\text{MoSe}_2/\text{MnO}_2$ nanocomposite. MoSe_2 and MnO_2 are characterized by band alignment, efficient charge separation, and visible light absorption, among other things. This material is unique because of its heterojunction structure, which enables efficient use of solar energy and boosts the generation of reactive oxygen species (ROS) to separate the pollutants. Along with the synthesis of components, there are band alignments. The easily accessible MoSe_2 and MnO_2 make the simple and eco-friendly method possible, the hydrothermal process provides a simple, scalable way to make $\text{MoSe}_2/\text{MnO}_2$ nanocomposites, and it allows for exact control over the materials composition and shape. When using this manufacturing process, nanocomposites may have their characteristics adjusted according to particular usages.

Up to Now, the unique $\text{MoSe}_2/\text{MnO}_2$ nanocomposites are very appealing for use in cleaning up the environment and treating wastewater. These novel materials maintain an advanced state because they are able to efficiently and sustainably solve the current problems with pollutant degradation, such as Direct Yellow (DY) degradation. In order to examine the practical applicability of the $\text{MoSe}_2/\text{MnO}_2$ nanocomposite, Reactive species trapping analysis studies were conducted with photocatalytic experiments. The major reactive species in

photocatalysis reaction were further determined, which in turn helped to clarify the complex reaction processes in photocatalysis. The hypothesis mechanism of improved overall photocatalytic degradation is illustrated and discussed in detail. This research shows that MoSe₂/MnO₂ nanocomposite could be used as high-tech, effective photocatalysts that are activated by visible light.

2. Experimental synthesis procedure

2.1. Chemical substances

Sodium molybdate (Na₂MoO₄) powder assay 98% is purchased from the SRL Pvt. Ltd. selenium powder block (Se) assay 99%, hydrazine hydrate (N₂H₄·H₂O) assay 99%, polyvinylpyrrolidone (PVP), Manganese sulphate (MnSO₄·H₂O) assay 99%, Potassium permanganate (KMnO₄) assay 99.99%, Direct yellow dye (DY) (C₂₆H₁₈N₄Na₂O₈S₂), were utilized for photocatalytic Process. We strictly adhered to the instructions and utilized only analytical-grade chemicals. Unless otherwise specified, we used lab-produced deionized (DI) water in the experiment.

2.2. Synthesis of MoSe₂

The synthesis of MoSe₂ is generally a hydrothermal process. Solution A involved 1.20 g of Na₂MoO₄ and 0.5 g of polyvinylpyrrolidone dissolving in 50 ml of DI water, followed by a 60 min magnetic stirred a solution containing particles equal to or below one-micron size with significant homogeneity. Then the soft solution of B was synthesised Se NPs by adding 30 ml of hydrazine (N₂H₄) with 0.4 g of selenium. We do it dropwise, slowly adding solution A to B until precipitation occurs. We then move the solution to a 100-ml Teflon-lined autoclave and keep it in an oven for one day at 200 °C. The crank did not yet fit the scoops, so the rotated them and washed away any residue particles with deionized water followed by ethanol. Then dried the byproduct at 80 °C for around 12 h and obtained a block-coloured powder.

2.3. Synthesis of MnO₂

At first, we used a simple hydrothermal route to synthesize MnO₂, using KMnO₄ and MnSO₄·H₂O as source materials. Step one was to sonicate MnSO₄·H₂O (0.9 g) with 25 mL of water. Next, we stirred the mixture with a magnetic stirrer and added 1.25 mg/mL of KMnO₄ dispersion in water to the mixture. After that, we place the solution into a 100-ml autoclave that has been imprinted with Teflon and oven it to 180°C for 24 hours. We dried

the powder in an oven at 60 °C for later use. MnO₂ was finally produced. Once we reached this stage, we sealed each prepared sample and fired it at 400 °C for 2 hours in a muffle furnace.

2.4. Synthesis of MoSe₂ /MnO₂ nanocomposite

Initially, we prepared MoSe₂ /MnO₂ nanocomposite by using hydrothermal process, typically 1.20 g of Na₂MoO₄ and 0.8 g of selenium (Se) to dissolve in 50 ml of DI water. Next, we individually mixed for 2.1 g of MnSO₄ and 1.96 g of KMnO₄ with 25 ml of deionized water and prepared the solution. Then we added both solutions drop by drop, continuously stirring the mixture for 1 hour. After that sonicating the mixture for 30 minutes, we place the solution into a 100-ml autoclave that has been imprinted with Teflon and oven it to 180°C for 24 hours. The remaining residue underwent multiple washes using ethanol and deionized water. It was subjected to drying in a hot air oven set at 80 °C for 12 hours, resulting in the acquisition of MoSe₂/MnO₂ nanocomposite. We detail the prepared sample and then use it to evaluate its photocatalytic performance and (Fig. 1) shows a simplified diagram of the chemical process of MoSe₂/MnO₂ nanocomposites.

2.5. Photocatalysis experiment

We investigated the photocatalytic activity of a nanocomposite of MoSe₂ and MnO₂ in the absence of direct sunlight. Therefore, we dissolved 0.5 g of MoSe₂/MnO₂ nanocomposites and 20 PPM of coloured dye in a 100-ml DI solution, then mixed them at room temperature for an hour. The mixture was stirred in darkness for 20 minutes, after which the adsorption-desorption equilibrium developed. Next, we exposed the photocatalyst suspension to ultraviolet (UV) and visible (Vis) light using a 500-watt halogen lamp [27], positioned 15 cm away from the surface of the DY photocatalyst mixture. Recirculating water from the water supply kept the photoreactor's temperature constant. We used a UV-Vis spectrometer to measure wavelengths between 200 and 800 nm along with the photoreactor to take out 15 ml of a dye-mixed solution at set times (every 30 minutes) for up to 120 minutes. We measured the absorbance at 395 nm to determine the DY concentrations in the samples. The experimental synthesis method and Eq. (1) allowed us to determine the DY degradation percentage.

$$\text{Degradation efficiency}(\%) = \frac{(C_0 - C)}{C_0} \times 100\% \dots\dots\dots (1)$$

In each case, C represents the initial DY dye concentration, and CO represents the final concentration. We used PXRD and SEM analysis to study the variations in crystal structure and morphology of the composite photocatalyst after four reuse experiments.

2.6. characterizations

We used powder X-ray diffraction analysis (Rigaku D/max ultra III diffractometer) and Cu k radiation (40 Kv, $\lambda = 0.154$ nm) to analyse the crystal structure of the MoSe₂/MnO₂ nanocomposite. We collected powder X-ray diffraction data between 10° and 80° theta degrees at room temperature. We used a Japanese device, the JASCO V-750, to capture the UV-vis spectra, which span a wavelength range of 200 to 800 nm. To understand the interplay between the nanocomposites, a Bruker tensor 27 FTIR spectrometer model was required. The samples were prepared for examination using a scanning electron microscope (JEOL JSM 7500F+) equipped with an electron detection system (EDS) set to 2.0 kV so that the forms could be seen. The research made use of a high-resolution transmission electron microscope (HR-TEM) performing at 200 kV, specifically a JEOL JEM-2100+. We studied the sizes of the materials to understand their forms.

3. Result and discussion

3.1. Characterization of Powder X-Ray diffraction

As shown in (Fig. 2) (a–c), PXRD was used to figure out the crystal structures and phase compositions of MoSe₂, MnO₂, and MoSe₂/MnO₂ samples. The MoSe₂ structure (JCPDS No. 01-077-1715) exhibited five distinct PXRD diffraction peaks at 13.3°, 13.6°, 37.8°, 42.2°, and 47.4°. These peaks accurately corresponded to the (002), (100), (103), (104), and (105) diffraction planes [28]. These peaks confirmed the hexagonal structure of MoSe₂. As noted in the pattern, the MoSe₂ exhibits distinct and strong peaks, indicating a higher degree of crystallinity in the samples. In addition to these strong peaks, the PXRD spectrum also shows other low-intensity peaks in the 20° to 30° range. Mo oxidised state causes these peaks. The main diffraction peaks may be due to MnO₂ (JCPDS No. 00-044-0141), with 2 Theta at 6.91°, 18.1°, 28.8°, 37.5°, 41.9°, 49.8°, 60.2° and 69.7°, which match the MnO₂ planes (110), (200), (310), (211), (301), (411), and (541) [29]. We can use the Debye-Scherrer formula, presented in Eq. (2), to determine the grain size (D). This formula is based on the full width at half maximum (FWHM) of typical crystalline peaks.

$$A = \frac{K\lambda}{\beta \cos\theta}$$

In this equation, the variable D is the size of the particle, k is the Scherrer constant (0.9), λ is the wavelength of the X-ray (1.5418 Å), and β is the entire width at half maximum of the specific diffraction angle (θ). The grain sizes on average of the samples MnO_2 , MoSe_2 , and $\text{MoSe}_2/\text{MnO}_2$ were estimated to be 20.05 nm, 19.92 nm, and 12.46 nm respectively. The decline in the crystallite size analytically advocates that there could be the reduction in the grain roughening in the $\text{MoSe}_2/\text{MnO}_2$ nano composite. Moreover, the MoSe_2 lattice constant of $a = b = 3.28$ Å, $c = 12.92$ Å, MnO_2 lattice constant of $a = b = 9.78$ Å, $c = 2.86$ Å respectively. In addition to these results, the lattice strain of the samples has been abbreviated to 0.0140, 0.0202, and 0.0070 respectively [30]. The PXRD pattern of $\text{MoSe}_2/\text{MnO}_2$ clearly shows the crystalline peaks of MoSe_2 and MnO_2 which confirmed that both patterns of shows in figure.

3.2. FTIR Spectroscopy analysis

The Fourier-transform infrared (FTIR) spectra of MoSe_2 and MnO_2 , measured in the range of 400-4000 cm^{-1} , are depicted in (Fig. 3) (a) and (b) respectively. The distinctive peaks detected at approximately 484 cm^{-1} , 556 cm^{-1} , 641 cm^{-1} , 781 cm^{-1} , 895 cm^{-1} , 1405 cm^{-1} and 1405 cm^{-1} correspond to the following chemical bonds: (Se-O-Se), (O-Mo-O), (M=O), (Se-O), (COOH), (Mo-OH), and (C-O) bonds, as well as C-H and O-H stretching vibrations, respectively [31]. MoSe_2 , possessing functional groups like (-OH) and (-COOH), exhibits a negatively charged surface, rendering it highly effective for the degradation of organic dyes. The nanostructured MnO_2 displayed three vibration bands below 1000 cm^{-1} , specifically at 508 cm^{-1} , and 623 cm^{-1} . Each of these vibrational bands is characteristic of the metal-oxygen bond within the MnO_6 octahedron, whether it involves the Mn-O or Mn-O-Mn bonding, and they exhibit good consistency with previously reported results [32]. In (Fig. 3) (c), the $\text{MoSe}_2/\text{MnO}_2$ nanocomposite exhibits shifted peaks corresponding to (Se-O-Se), (O-Mo-O), (M=O), (Se-O), (Mo-OH) and (Mn-O) or (Mn-O-Mn) bonds, which are located at 453 cm^{-1} , 609 cm^{-1} , 736 cm^{-1} , 802 cm^{-1} , 1362 cm^{-1} and 514 cm^{-1} , 611 cm^{-1} respectively. Both PXRD and FTIR analysis results provide complementary information, confirming the structural and functional characteristics of the $\text{MoSe}_2/\text{MnO}_2$ nanocomposite simultaneously.

3.3. UV-Vis analysis

The UV-Vis spectra of the synthesized samples are depicted in (Fig. 4) (a). The absorption peaks for MoSe₂ were observed at wavelengths of 341 nm, 589 nm, and 664 nm respectively [33]. Likewise, the absorption peaks for MnO₂ were observed at wavelengths of 260 nm, 410 nm, and 511 nm, respectively [34] where as for the MoSe₂/MnO₂ composite, shifted peaks were observed at 271 nm, 395 nm, 516 nm, and 664 nm respectively. It is noteworthy to mention that the sample containing MoSe₂/MnO₂ exhibits the largest absorption peak, indicative of a synchronized effect between the two components. Thus, the band gap values may be inferred from the $\alpha h\nu_2$ (Tauc's plot) using the equation: $\alpha(h\nu)_2 = \text{const} (h\nu - E_g)^{1/2}$. The absorption coefficient, Planck's constant, the incident light frequency, and the band gap are represented by α , h , ν , and E_g , respectively [35]. (Fig. 4) (b) and (c) illustrates an estimated optical band gap by using Tauc's plot relations. The calculated bandgap for MoSe₂, MnO₂ and MoSe₂/MnO₂ nanocomposite were 1.96 eV, 2.52 eV, and 2.73 eV, respectively. The observed band narrowing in the MoSe₂/MnO₂ nanocomposite indicates that the combination can effectively capture a broader spectrum of visible light, including direct sunlight. The enhanced absorption of visible light contributes to the reduction in bandgap observed in the MoSe₂/MnO₂ nanocomposite. This is believed to enhance the photocatalytic efficiency of the material when exposed to UV-visible light.

3.4. Morphology analysis

The SEM images of MoSe₂ and MoSe₂/MnO₂ were shown in (Fig. 5) The prepared samples display nanoparticles that are randomly oriented and interconnected, forming a 0D network, as illustrated in (Fig. 5) (a) and (b). The surfaces generally appear smooth, and the diameters of the nanoparticles are similar. In (Fig. 5) (c) and (d), it is evident that the highly localized MoSe₂ nanoparticles are uniformly distributed throughout the MnO₂ nanostructure. The MoSe₂/MnO₂ nanocomposite exhibits a particle with nanoflakes-like structure. The photocatalytic processes of these materials stand to benefit from their large surface area, high light-collecting capacity, and efficient charge mobility [36,37]. Also, it's important to note that altering the quantities of reactants for MoSe₂ and MoSe₂/MnO₂ composite allows effective control over the form of MoSe₂ on particles with nanoflakes-like structures. Additionally, the quantity of MoSe₂ on the particles with nanoflakes-like structure was also enhanced during the same periods, as confirmed by the X-ray (EDX) spectra in (Fig. 6) (a) and (b) and the atomic ratios provided in the table. Additionally, both MoSe₂ and MoSe₂/MnO₂ nanocomposite particles with nanoflakes-like were synthesized using the same hydrothermal process.

The HR-TEM images of both MoSe₂ and MoSe₂/MnO₂ nanocomposite were depicted in (Fig.7) (a-h). Notably, thin and small nanoparticle structures with MoSe₂ layers were visible in the prepared MoSe₂, as observed in the HR-TEM image captured from the sample edge. A substantial aggregation of MoSe₂, as depicted in the shaded area of the figure, suggests the successful synthesis of numerous thin MoSe₂ layers using a straight forward hydrothermal method. This observation aligns with the morphology reported in the existing literature [36]. (Fig.7) (e-h) display TEM images of MoSe₂/MnO₂ nanocomposites. As per the HR-TEM image, the prepared nanocomposite exhibited a distinct crystal structure. As anticipated, the measured d-spacing of 0.67 nm corresponds to the same value as the MoSe₂ (002) interplanar spacing. Additionally, the observed d-spacing of 0.32 nm aligns with the (110) lattice of the MnO₂ nanostructure [38]. The successful formation of the MoSe₂/MnO₂ composite was confirmed by the close binding of their lattice fringes, indicating a strong interaction between the two materials. This interaction significantly enhances the electric structure at the interface, making it easier for charge carriers to separate [39]. Furthermore, the composite (002) lattice spacing of 0.70 nm for MoSe₂ was notably larger than the 0.67 nm corresponding to the (002) plane in standard MoSe₂. This discrepancy could be attributed to the replacement of Se at the Se site by O and the incorporation of O into the MoSe₂ structure.

To provide additional insight into the HR-TEM, also known as Energy Dispersive X-ray Spectroscopy (EDS) mapping of the composites was conducted and is depicted in (Fig. 8) (a–f). The EDS mapping reveals the presence of four elements in the composite: Mo, Se, Mn, and O. This shows that the composite MoSe₂ and MnO₂ were well-combined, and that the distribution of the four components was consistent. The effective mobility of photocarriers was made possible by the strong contact between MoSe₂ and MnO₂, enhancing the effectiveness of the direct photocatalytic process.

3.5. X-ray photoelectron spectroscopy (XPS)

(Fig. 9) shows the results of the XPS analysis of MoSe₂/MnO₂ elemental composition and binding energy. The XPS spectra of the nanocomposite MoSe₂/MnO₂ showed peaks for the C, O, Mn, Mo, and Se elements. It is possible that adventitious oxygen is responsible for the O 1S signal at 529.87 eV. One common calibration standard is the O 1S peak, which typically corresponds to the binding energy of oxygen atoms in a material. A Mo 3D embedded pattern is present in pure MoSe₂. It is feasible to assign these molecular orbitals to

the following elements Mo 4⁺ at 229.0 eV and Mo 3d_{3/2} at 232.2 eV, Mo 5⁺ at 233.0 eV and Mo 3d_{3/2} at 230.3 eV, and Mo 6⁺ at 235.9 eV and 233.8 eV. There have been reports [40]. that the two peaks at 54.6 eV and 55.4 eV in the high-resolution Se 3d spectra of MoSe₂ are related to the Se 3d_{5/2} and Se 3d_{3/2} of Se in MoSe₂. We obtained the XPS spectra of Mo 3d, Se 3d, and Mn 2p, which we show in (Fig. 9) (a–f) in that order. (Fig. 9) (b–c) shows the MoSe₂ shifted peaks at 232.1 eV and 235.1 eV, respectively, for Mo 3d_{5/2} and Mo 3d_{3/2}. Together, they provide a suitable match for the MoSe₂ (4⁺) chemical states. It was clear from the Se 3d_{5/2} and Se 3d_{3/2} shifted peaks of MoSe₂ at 49.8 eV and 48.2 eV that the Se atoms were in an oxidation chemical state 2 [41]. These are the Mn 2p_{3/2}, Mn 2p_{1/2}, and chemical state of atom Mn⁴⁺ peaks for the MnO₂. They are also at 640 eV, 652.5 eV, and 642.2 eV. The results align with previous publications [42]. (Fig 9) (d) displays the high-resolution MnO₂ XPS Mn 2p spectrum. The two shifted peaks of 2p_{3/2} (640.6 eV) and 2p_{1/2} (652.5 eV) for Mn moved in correspondence with the change in the electronic state of Mn⁴⁺ [39]. The presence of MnO₂ in MoSe₂ validated it.

In particular, the composite Mo 3d and Se 3d peaks, together with its Mn 2p peaks, moved towards lower binding energies. Thus, it is clear that there is a strong interaction between the MoSe₂/MnO₂ nanocomposites [43]. Also, the O1-S spectra could show three peaks. As shown in (Fig. 9) (e) [44]. the peaks at 529.8 eV, 531.0 eV, and 532.4 eV came from the lattice oxygen (Mn-O-Mn) surface absorption hydroxyl groups (Mn-OH) and water that was taken in by the material's surface. The C1 S signals are broken down into three Gaussian peaks, as shown in (Fig. 9) (f), so that different chemical states of carbon atoms can be found. At 284.4 eV, there is a prominent peak 2 that represents the binding energy of carbon atoms in the carbon-carbon structure. The tiny peaks at 285.9 eV and 288.5 eV, respectively, represent the carbon binding energies from the C-O bond and the C=O-C bond [45]. With the addition, the hydroxyl group peak shifted slightly towards a higher binding energy. This indicates that the MoSe₂/MnO₂ nanocomposite has a reduced electron density of the surface hydroxyl groups. The nearby MoSe₂/MnO₂ nanocomposite may help to explain this observation. It is interesting to note that the surface of the composite has a lot more hydroxyl groups, which may help it absorb contaminants better by creating hydrogen and also help photogeneration holes (h⁺) by giving them electrons. Additionally, the oxidation of these holes to OH could enhance the separation of photogenerated carriers and enhance the photocatalytic process.

3.6. Light absorption and photocatalytic properties

As a model pollutant, we utilised an organic dye (DY) Direct Yellow to evaluate the photocatalytic performance of the photocatalyst. The photodegradation activity took place when exposed to under UV-Vis light. (Fig. 10) (a-f) shows the UV-Vis absorbance spectrum of DY dye degrading is (a) MoSe₂, (b) MnO₂, and (c) MoSe₂/MnO₂ at 120 minutes. The absorption of dye solution doesn't change the optimal conditions for absorption and release in large quantities (Fig. 10) (d) displays the photo standard behaviour of the DY dye as analysed in a black experiment with the photocatalyst adsorption. The MoSe₂, MnO₂ and MoSe₂/MnO₂ nanocomposite are added to the DY dye solution, and the solution is investigated for 120 min. In comparison to MoSe₂, the MoSe₂/MnO₂ nanocomposite demonstrates enhanced catalytic performance for the degradation of DY dye when exposed to under UV-Vis light.

The kinetics of the photocatalytic degradation of DY dye were assessed using Equation (2),

$$\ln \frac{C_t}{C_0} = -kt \dots\dots\dots (2)$$

The initial and final concentrations of the DY dye are C₀ and C_t, respectively, and k represents the pseudo-first-order rate constant (min⁻¹). In Figure 10, we can see the pseudo-first-order kinetics. These are displayed in Table 3: First, the amount of dye in parts per million; second, the rate of degradation in percentage; third, the kinetic equation; fourth, the rate constant in units of k; fifth, the time in minutes; and finally, the R² values of the MoSe₂, MnO₂, and MoSe₂/MnO₂ mix. The table's data provides the basis for our analysis. 3. While MnO₂ showed a rate constant of 0.0136 min⁻¹ and MoSe₂/MnO₂ showed a rate constant of 0.1294 min⁻¹, MoSe₂ showed a rate constant of 0.0290 min⁻¹. Its shape was believed to be responsible for the increased photocatalytic activity of MoSe₂/MnO₂. A higher surface area activation rate is directly proportional to a higher reactive oxygen species production rate, since photocatalysis is a surface event. Because it dissolves in DI water, the MnO₂ catalyst enhances the interaction between DY molecules. This resulted in a greater photocatalytic efficiency for MoSe₂/MnO₂ than for MoSe₂ alone. Thus, MoSe₂/MnO₂ outperformed MoSe₂ in terms of photocatalytic efficiency. (Fig. 10) (f) illustrates the degradation performance of UV-Vis light-induced photocatalysis. In the as-made materials, MoSe₂/MnO₂ had a photocatalytic degradation efficiency of 96%. Additional research showed that the combination of MoSe₂ and MnO₂ maintained its outstanding photocatalytic and adsorption properties. More durable, more adsorption and photocatalytic activity, and a slightly lower

adsorption and photocatalytic synergistic reduction rate than Direct Yellow (DY), the MoSe₂/MnO₂ composite showed some promise.

Some tests (Fig. 11a) looked at how EDTA, BQ, and IPA, three oxidative species known to remove OH*, O₂*, and free electrons, respectively, changed how DY broke down and dropped. MoSe₂/MnO₂, acting as a photocatalyst, effectively destroyed 98.4% of DY, even in the absence of scavengers. We recorded the following DY disappearance rates in the present scavenger concentrations IPA = 59.2%, BQ = 65.8%, and EDTA = 38.4%. The results indicate that OH* is the primary cause of the photocatalytic oxidation of MB. We have shown that the effects of free electrons and O₂* on deterioration are insignificant.

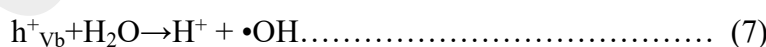
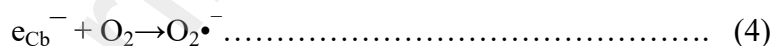
Additionally, we conducted four independent photocatalysis experiments to further explore the possibility of reusing MoSe₂/MnO₂ nanocomposites. As seen in (Fig.11b), the photocatalytic efficacy remained almost constant across all four cycles. (Fig.11c) shows the recovery and XRD analysis of the MoSe₂/MnO₂ sample after four reuse cycles. The XRD results were identical in the reused and as-prepared MoSe₂/MnO₂ samples, suggesting that the crystalline structure was unaltered. Consequently, repeated photocatalytic studies proved the stability and dependability of the MoSe₂/MnO₂ nanocomposite.

3.7. Photocatalytic mechanism of MoSe₂/MnO₂ Nanocomposite

(Fig.12) illustrates a potential photocatalytic mechanism under irradiation. The observed changes in photocatalytic activity are attributed to variations in phase growth and morphological alterations associated with reduction and oxidation processes. The photocatalytic mechanism typically involves three main steps: (i) The process of absorbing the photons that possess energy levels beyond the bandgap of the photocatalyst; (ii) The process of electron-hole pairs being separated, migrating, or recombining respectively; and (iii) redox reactions occurring at the surface of the photocatalyst. In general, surface imperfections can serve as sites for the absorption of oxygen and water. Semiconductor photocatalysts, when exposed to air or oxygen, can effectively degrade numerous organic pollutants. When activated by UV-Vis light (hν), MoSe₂/MnO₂ generates electron-hole pairs, which act as strong antioxidants and reducing agents. The photocatalyst exhibits efficient performance because holes and photovoltaic electrons do not readily recombine on the surface of the semiconductor. The following expressions outline the photocatalytic mechanisms for the degradation of DY dyes (3)-(9). To enhance photocatalytic activity, the

electrons that are produced by light generated in an oxidation-reduction process previous recombination. The production of the pairs of electron-holes in MoSe₂/MnO₂ nanocomposite in the absence of UV-Vis light is an accelerated oxidation process in which electrons are activated from VB via substantial light absorption Eq (3). However, when oxygen molecules are absorbed by the excited electrons (e_{cb}⁻), a number of reactive substances are formed, containing radicals such as hydrogen peroxide (H₂O₂), hydroxyl (•OH) radicals, and superoxide (•O₂⁻) Eq (4-6)[46]

The formation of highly oxidizable positively charged holes (h_{VB}⁺) under visible light, on the other together, indicates that their source might instantly carry out the oxidative degradation of a yellow dye. Further, a different component of the holes known as h_{VB}⁺ combines with the absorbed H₂O and OH⁻ in the DY solution to produce hydroxyl (•OH) radicals (Eq. 7 and 8). This leads to the outcome described in reference [47]. A powerful oxidant, hydroxyl radicals (•OH) may be converted into water and carbon dioxide, two substances that are good for the environment. Eq. (9). MoSe₂/MnO₂ induces of •OH radicals and also contributes to the advancement of the dye degradation process. The shortage of super oxide emit can also be seen in the measurements. So, this means that hydroxyl radicals make it possible for the dye degradation. Overall, it was determined that the synthetic MoSe₂/MnO₂ composite that has been created showed strong photocatalytic activity in the presence of UV light. As a result of influence of the synthesised factor such as quantum confinement, sample size and the catalyst, the energy band gap as the continuously grows in thickness as it approaches the nanoscale. Additionally, the generated photocatalysts' performance in degrading organic pollutants was similar to that of the prior study and it's shown in Table 4. In (Fig. 12) the proposed photocatalytic mechanism of MoSe₂/MnO₂ for the degradation of (DY) Direct yellow dye is depicted schematically.





4. Conclusion

Our group has been successfully synthesized a MoSe₂/MnO₂ nanocomposite by using simple hydrothermal method, which significantly enhances its photocatalytic activity. The PXRD peaks are corresponding to the individual components of pure MoSe₂, MnO₂ and MoSe₂/MnO₂ nanocomposite confirmed and then existence of intermolecular interaction between nanocomposites. The characteristic studies of FTIR spectroscopy further supported the MoSe₂/MnO₂ nanocomposite formation. UV-Vis absorbance spectroscopy was used to optical band gap calculated to using Tauc's plots indicated the band gap of MoSe₂ 1.96 eV, MnO₂ 2.73 eV, and MoSe₂/MnO₂ 2.52 eV respectively. From the result of morphologies studies on SEM and HR-TEM for MoSe₂, MnO₂ and MoSe₂/MnO₂ nanocomposite were confirmed particles with nanoflakes-like structure. The excellent photocatalytic efficiency performed by pure and nanocomposite was due to the high surface area, stable and same interface contact, accelerated electron movement under UV-Vis light in photocatalytic degradation of Direct Yellow (DY) is seen to be 96% of nanocomposite material than of pure MoSe₂ and MnO₂.

Data availability Data

Data will be made available on request.

Preprint not peer reviewed

References

- [1] X. Sun, H. Huang, Q. Zhao, T. Ma, L. Wang, Thin-Layered Photocatalysts, *Adv Funct Mater* 30 (2020). <https://doi.org/10.1002/adfm.201910005>.
- [2] W. Shang, W. Liu, X. Cai, J. Hu, J. Guo, C. Xin, Y. Li, N. Zhang, N. Wang, C. Hao, Y. Shi, Insights into atomically dispersed reactive centers on g-C₃N₄ photocatalysts for water splitting, *Advanced Powder Materials* 2 (2023). <https://doi.org/10.1016/j.apmate.2022.100094>.
- [3] H. Gong, L. Wang, K. Zhou, D. Zhang, Y. Zhang, V. Adamaki, A. Sergejevs, C. Bowen, Improved photocatalytic performance of gradient reduced TiO₂ ceramics with aligned pore channels, *Advanced Powder Materials* 1 (2022). <https://doi.org/10.1016/j.apmate.2021.11.011>.
- [4] J. Ma, X. Li, Y. Li, G. Jiao, H. Su, D. Xiao, S. Zhai, R. Sun, Single-atom zinc catalyst for co-production of hydrogen and fine chemicals in soluble biomass solution, *Advanced Powder Materials* 1 (2022). <https://doi.org/10.1016/j.apmate.2022.100058>.
- [5] Y. Zheng, L. Lin, B. Wang, X. Wang, Polymeres graphitisches Kohlenstoffnitrid für die nachhaltige Photoredoxkatalyse, *Angewandte Chemie* 127 (2015) 13060–13077. <https://doi.org/10.1002/ange.201501788>.
- [6] Y. Zhu, Y. Feng, S. Chen, M. Ding, J. Yao, Carbon nitride nanotube-based materials for energy and environmental applications: a review of recent progresses, *J Mater Chem A Mater* 8 (2020) 25626–25648. <https://doi.org/10.1039/d0ta08892g>.
- [7] H. Wang, X. Zhang, Y. Xie, Photoresponsive polymeric carbon nitride-based materials: Design and application, *Materials Today* 23 (2019) 72–86. <https://doi.org/10.1016/j.mattod.2018.05.001>.
- [8] D. Zhang, W. He, J. Ye, X. Gao, D. Wang, J. Song, Polymeric Carbon Nitride-Derived Photocatalysts for Water Splitting and Nitrogen Fixation, *Small* 17 (2021). <https://doi.org/10.1002/sml.202005149>.
- [9] M. Li, J. Sun, G. Chen, S. Wang, S. Yao, Inducing photocarrier separation via 3D porous faveolate cross-linked carbon to enhance photothermal/pyroelectric property, *Advanced Powder Materials* 1 (2022). <https://doi.org/10.1016/j.apmate.2022.01.005>.

- [10] D. Liang, Y. Huang, F. Wu, J. Luo, X. Yi, J. Wang, X. Qiu, In situ synthesis of gC_3N_4/TiO_2 with {001} and {101} facets coexposed for water remediation, *Appl Surf Sci* 487 (2019) 322–334. <https://doi.org/10.1016/j.apsusc.2019.05.088>.
- [11] J. Wen, G. Wang, P. Hao, X. Li, W. Liu, X. Chen, H. Zhan, F. Li, Nongraphitic Carbon Nitride Melem Oligomer Nanosheets for Photocatalytic Degradation of Organic Pollutants, *ACS Appl Nano Mater* (2022). <https://doi.org/10.1021/acsanm.2c03473>.
- [12] X. Shen, T. Zhang, P. Xu, L. Zhang, J. Liu, Z. Chen, Growth of C_3N_4 nanosheets on carbon-fiber cloth as flexible and macroscale filter-membrane-shaped photocatalyst for degrading the flowing wastewater, *Appl Catal B* 219 (2017) 425–431. <https://doi.org/10.1016/j.apcatb.2017.07.059>.
- [13] B. Fang, Z. Xing, D. Sun, Z. Li, W. Zhou, Hollow semiconductor photocatalysts for solar energy conversion, *Advanced Powder Materials* 1 (2022). <https://doi.org/10.1016/j.apmate.2021.11.008>.
- [14] H. Wang, Y. Xu, D. Xu, L. Chen, X. Qiu, Y. Zhu, Graphitic Carbon Nitride for Photoelectrochemical Detection of Environmental Pollutants, *ACS ES and T Engineering* 2 (2022) 140–157. <https://doi.org/10.1021/acsestengg.1c00337>.
- [15] P. Kumar, D. Laishram, R.K. Sharma, A. Vinu, J. Hu, M.G. Kibria, Boosting Photocatalytic Activity Using Carbon Nitride Based 2D/2D van der Waals Heterojunctions, *Chemistry of Materials* 33 (2021) 9012–9092. <https://doi.org/10.1021/acs.chemmater.1c03166>.
- [16] H. Wang, Y. Xu, D. Xu, L. Chen, Q. Xiao, X. Qiu, Cu (II)-Grafted Carbon Nitride Quantum Dots with High Crystallinity for Photoelectrochemical Detection Application, *Ind Eng Chem Res* (2022). <https://doi.org/10.1021/acs.iecr.2c00525>.
- [17] H. Mittal, M. Khanuja, Nanosheets-and nanourchins-like nanostructures of $MoSe_2$ for photocatalytic water purification: kinetics and reusability study, (n.d.). <https://doi.org/10.1007/s11356-019-06275-8/Published>.
- [18] M. Wang, Z. Peng, J. Qian, H. Li, Z. Zhao, X. Fu, Highly efficient solar-driven photocatalytic degradation on environmental pollutants over a novel C fibers@ $MoSe_2$

- nanoplates core-shell composite, *J Hazard Mater* 347 (2018) 403–411. <https://doi.org/10.1016/j.jhazmat.2018.01.013>.
- [19] Q. Jiang, Y. Lu, Z. Huang, J. Hu, Facile solvent-thermal synthesis of ultrathin MoSe₂ nanosheets for hydrogen evolution and organic dyes adsorption, *Appl Surf Sci* 402 (2017) 277–285. <https://doi.org/10.1016/j.apsusc.2017.01.049>.
- [20] N. Chaudhary, M. Khanuja, Architectural Design of Photodetector Based on 2D (MoS₂ Nanosheets)/1D (WS₂ Nanorods) Heterostructure Synthesized by Facile Hydrothermal Method, *J Electrochem Soc* 166 (2019) B1276–B1285. <https://doi.org/10.1149/2.0341914jes>.
- [21] N. Chaudhary, M. Khanuja, Abid, S.S. Islam, Hydrothermal synthesis of MoS₂ nanosheets for multiple wavelength optical sensing applications, *Sens Actuators A Phys* 277 (2018) 190–198. <https://doi.org/10.1016/j.sna.2018.05.008>.
- [22] I. Siddiqui, H. Mittal, V.K. Kohli, P. Gautam, M. Ali, M. Khanuja, Hydrothermally synthesized micron sized, broom-shaped MoSe₂ nanostructures for superior photocatalytic water purification, *Mater Res Express* 5 (2018). <https://doi.org/10.1088/2053-1591/aae241>.
- [23] H. Mittal, A. Kumar, M. Khanuja, In-situ oxidative polymerization of aniline on hydrothermally synthesized MoSe₂ for enhanced photocatalytic degradation of organic dyes, *Journal of Saudi Chemical Society* 23 (2019) 836–845. <https://doi.org/10.1016/j.jscs.2019.02.004>.
- [24] J. Narang, A. Mishra, R. Pilloton, A. Vv, S. Wadhwa, C.S. Pundir, M. Khanuja, Development of MoSe₂ nano-urchins as a sensing platform for a selective bio-capturing of Escherichia coli Shiga toxin DNA, *Biosensors (Basel)* 8 (2018). <https://doi.org/10.3390/bios8030077>.
- [25] V.K. Parida, S.K. Srivastava, S. Chowdhury, A.K. Gupta, Facile synthesis of 2D/0D Bi₂O₃/MnO₂ Z-scheme heterojunction for enhanced visible light-assisted photocatalytic degradation of acetaminophen, *Chemical Engineering Journal* 472 (2023). <https://doi.org/10.1016/j.cej.2023.144969>.
- [26] V.K. Parida, S.K. Srivastava, S. Chowdhury, A.K. Gupta, Visible Light-Assisted Degradation of Sulfamethoxazole on 2D/0D Sulfur-Doped Bi₂O₃/MnO₂ Z-Scheme

- Heterojunction Immobilized Photocatalysts, *Langmuir* 39 (2023) 18846–18865. <https://doi.org/10.1021/acs.langmuir.3c02733>.
- [27] L. Liang, Z. Mo, N. Li, H. Liu, G. Feng, A. Wei, Hydrothermal Synthesis of The Flower-Like MoS₂ Nanosheets Microspheres and Its Photocatalytic Degradation Of Methyl Orange, 2020.
- [28] J. Sawadogo, M. Bougouma, J. Legma, M. Ogletree, Determination of stoichiometry from polycrystalline powders of transition metals lamellar dichalcogenides: MoSe₂, WSe₂, obtained by synthesis in laboratory, *Int J Biol Chem Sci* 9 (2015) 454. <https://doi.org/10.4314/ijbcs.v9i1.39>.
- [29] C. Shi, G.L. Zang, Z. Zhang, G.P. Sheng, Y.X. Huang, G.X. Zhao, X.K. Wang, H.Q. Yu, Synthesis of layered MnO₂ nanosheets for enhanced oxygen reduction reaction catalytic activity, *Electrochim Acta* 132 (2014) 239–243. <https://doi.org/10.1016/j.electacta.2014.03.150>.
- [30] T. Elangovan, P. Kuppusami, R. Thirumurugesan, C. Sudha, E. Mohandas, D. Mangalaraj, A study on the influence of copper content in Cr N/Cu nanocomposite thin films prepared by pulsed dc magnetron sputtering, in: *J Nanosci Nanotechnol*, 2009: pp. 5436–5440. <https://doi.org/10.1166/jnn.2009.1129>.
- [31] I. Siddiqui, H. Mittal, V.K. Kohli, P. Gautam, M. Ali, M. Khanuja, Hydrothermally synthesized micron sized, broom-shaped MoSe₂ nanostructures for superior photocatalytic water purification, *Mater Res Express* 5 (2018). <https://doi.org/10.1088/2053-1591/aae241>.
- [32] M.F. Warsi, M. Bilal, S. Zulfiqar, M.U. Khalid, P.O. Agboola, I. Shakir, Enhanced visible light driven Photocatalytic activity of MnO₂ nanomaterials and their hybrid structure with carbon nanotubes, *Mater Res Express* 7 (2020). <https://doi.org/10.1088/2053-1591/abfb8d>.
- [33] H. Mittal, A. Ivaturi, M. Khanuja, MoSe₂-modified ZIF-8 novel nanocomposite for photocatalytic remediation of textile dye and antibiotic-contaminated wastewater, *Environmental Science and Pollution Research* 30 (2023) 4151–4165. <https://doi.org/10.1007/s11356-022-22487-x>.

- [34] S. Vijayalakshmi, E. Kumar, Synthesis and Investigations on structural, optical, thermal and electrical conductivity of α - MnO_2 nanoparticles, 2019. <https://www.researchgate.net/publication/335397323>.
- [35] S.M. EL-Dafrawy, M. Tarek, S. Samra, S.M. Hassan, Synthesis, photocatalytic and antidiabetic properties of ZnO/PVA nanoparticles, *Sci Rep* 11 (2021). <https://doi.org/10.1038/s41598-021-90846-8>.
- [36] Z. Lu, D. Zeng, H. Zheng, Q. Liu, X. Gao, X. He, L. Wei, W.J. Ong, Enhanced interfacial electron transfer and boosted visible-light photocatalytic hydrogen evolution activity of g- C_3N_4 by noble-metal-free MoSe_2 nanoparticles, *J Mater Sci* 55 (2020) 13114–13126. <https://doi.org/10.1007/s10853-020-04945-4>.
- [37] M.F. Warsi, M. Bilal, S. Zulfiqar, M.U. Khalid, P.O. Agboola, I. Shakir, Enhanced visible light driven Photocatalytic activity of MnO_2 nanomaterials and their hybrid structure with carbon nanotubes, *Mater Res Express* 7 (2020). <https://doi.org/10.1088/2053-1591/abfb8d>.
- [38] S. Rong, T. He, P. Zhang, Self-assembly of MnO_2 nanostructures into high purity three-dimensional framework for high efficiency formaldehyde mineralization, *Appl Catal B* 267 (2020). <https://doi.org/10.1016/j.apcatb.2019.118375>.
- [39] J. Zhang, Y. Hu, H. Zheng, P. Zhang, Hierarchical Z-scheme 1D/2D architecture with TiO_2 nanowires decorated by MnO_2 nanosheets for efficient adsorption and full spectrum photocatalytic degradation of organic pollutants, *Catal Sci Technol* 10 (2020) 3603–3612. <https://doi.org/10.1039/d0cy00419g>.
- [40] H. Chu, X. Liu, B. Liu, G. Zhu, W. Lei, H. Du, J. Liu, J. Li, C. Li, C. Sun, Hexagonal 2H- MoSe_2 broad spectrum active photocatalyst for Cr (VI) reduction, *Sci Rep* 6 (2016). <https://doi.org/10.1038/srep35304>.
- [41] J. Lu, D.L. Bao, K. Qian, S. Zhang, H. Chen, X. Lin, S.X. Du, H.J. Gao, Identifying and Visualizing the Edge Terminations of Single-Layer MoSe_2 Island Epitaxially Grown on Au (111), *ACS Nano* 11 (2017) 1689–1695. <https://doi.org/10.1021/acsnano.6b07512>.
- [42] A.E. Reddy, T. Anitha, C.V.V.M. Gopi, S. Srinivasa Rao, C.V. Thulasi-Varma, D. Punnoose, H.J. Kim, Fabrication of a snail shell-like structured $\text{MnO}_2@ \text{CoNiO}_2$

- composite electrode for high performance supercapacitors, *RSC Adv* 7 (2017) 12301–12308. <https://doi.org/10.1039/c7ra01126a>.
- [43] X. Li, K. Peng, MoSe₂/montmorillonite composite nanosheets: Hydrothermal synthesis, structural characteristics, and enhanced photocatalytic activity, *Minerals* 8 (2018). <https://doi.org/10.3390/min8070268>.
- [44] Z. Li, W. Kang, Z. Han, J. Yan, B. Cheng, Y. Liu, Hierarchical MnOx@PVDF/MWCNTs tree-like nanofiber membrane with high catalytic oxidation activity, *J Alloys Compd* 780 (2019) 805–815. <https://doi.org/10.1016/j.jallcom.2018.11.405>.
- [45] L. Huang, X. Luo, C. Chen, Q. Jiang, A high specific capacity aqueous zinc-manganese battery with a ε-MnO₂ cathode, *Ionics (Kiel)* 27 (2021) 3933–3941. <https://doi.org/10.1007/s11581-021-04160-4>.
- [46] H. Mittal, M. Khanuja, Nanosheets-and nanourchins-like nanostructures of MoSe₂ for photocatalytic water purification: kinetics and reusability study, (n.d.). <https://doi.org/10.1007/s11356-019-06275-8/Published>.
- [47] H. Mittal, M. Khanuja, Nanosheets-and nanourchins-like nanostructures of MoSe₂ for photocatalytic water purification: kinetics and reusability study, (n.d.). <https://doi.org/10.1007/s11356-019-06275-8/Published>.
- [48] D. Monga, S. Basu, Tuning the photocatalytic/electrocatalytic properties of MoS₂/MoSe₂ heterostructures by varying the weight ratios for enhanced wastewater treatment and hydrogen production, *RSC Adv* 11 (2021) 22585–22597. <https://doi.org/10.1039/d1ra01760h>.
- [49] G. Khabiri, A.M. Aboaraia, M. Soliman, A.A. Guda, V. V. Butova, I.S. Yahia, A. V. Soldatov, A novel α-Fe₂O₃@MoS₂ QDs heterostructure for enhanced visible-light photocatalytic performance using ultrasonication approach, *Ceram Int* 46 (2020) 19600–19608. <https://doi.org/10.1016/j.ceramint.2020.05.021>.
- [50] J. Zhang, X. Zan, X. Shen, H. Zheng, Preparation of direct Z-scheme hierarchical MoS₂/MnO₂ composite for efficient adsorption and wide spectrum photocatalytic degradation of organic pollutants in water, n.d. <https://ssrn.com/abstract=4279267>.

- [51] J. Zhao, J. Nan, Z. Zhao, N. Li, J. Liu, F. Cui, Energy-efficient fabrication of a novel multivalence $\text{Mn}_3\text{O}_4\text{-MnO}_2$ heterojunction for dye degradation under visible light irradiation, *Appl Catal B* 202 (2017) 509–517. <https://doi.org/10.1016/j.apcatb.2016.09.065>.
- [52] X. Zheng, Z. Han, W. Yang, F. Qu, B. Liu, X. Wu, 3D $\text{Co}_3\text{O}_4\text{@MnO}_2$ heterostructures grown on a flexible substrate and their applications in supercapacitor electrodes and photocatalysts, *Dalton Transactions* 45 (2016) 16850–16858. <https://doi.org/10.1039/c6dt03076a>.